One-step synthesis of Ag-Cu bimetallic nanoparticles on p-Si photoelectrodes for solar-driven CO 2 reduction

Harsh Chaliyawala, Stéphane Bastide, Diane Muller-Bouvet, Christophe Pichon, Kadiatou Bah, Anffane Djoumoi, Frédéric Marty, Tarik Bourouina, E. Torralba

One-step synthesis of Ag-Cu bimetallic nanoparticles on p-Si photoelectrodes for solar-driven CO_2 reduction

Harsh A. Chaliyawala[1], Stephane Bastide[1], Diane Muller-Bouvet[1], Christophe Pichon, Kadiatou Bah[1], Anffane Djoumoi[1], Frédéric Marty[2], Tarik Bourouina[2], Encarnacion Torralba[1*]*

[1]Univ Paris Est Creteil, CNRS, ICMPE, UMR 7182, 2 rue Henri Dunant, 94320 Thiais, France

[2]ESYCOM - Electronique, Systèmes de communication et Microsystèmes (Université de Paris-Est - Marne-la-Vallée) Cité Descartes, 77454 Marne-la-Vallée Cedex 2, France

Abstract

In the present work, we report the one-step synthesis of Ag_xCu_{100-x} bimetallic nanoparticles (NPs) on p-type silicon (p-Si) supports and their application as photocathodes for the photoelectrochemical CO_2 reduction reaction (PEC-CO_2RR). Based on the metal-assisted chemical etching (MACE) of Si in HF medium, the proposed method allows the formation of NPs homogeneously distributed on the Si surface, with an excellent control of their bimetallic composition, surface coverage and morphology by adjusting the experimental conditions (deposition time, precursor concentrations). Microstructural studies reveal a phase-separated polycrystalline structure for the bimetallic with a high dispersion of Ag and Cu nanocrystallites, remarkable for Ag/Cu nanostructures synthesized by soft chemistry.

The analysis of the PEC-CO_2RR shows a better performance of $Ag_{50}Cu_{50}$/p-Si than Ag/p-Si and Cu/p-Si, with an onset potential shift of 840 mV and a ratiometric power saved of ~3% compared to an analogous metal electrode in CO_2 saturated 0.5 M $NaHCO_3$. Photoelectrolysis tests under 1 sun illumination coupled with gas chromatography demonstrate the capacity of the bimetallic photocathode to guide the selectivity with the applied potential. Thus, CO_2 conversion to CO and CH_4 are achieved on $Ag_{50}Cu_{50}$/p-Si, with a maximum Faradaic efficiency (FE) of 26 % and 18.2% at -0.72 and -0.87 V_{RHE}, respectively. These values are consistent with recent research on Ag-Cu systems on Si for PEC-CO_2RR but

* Corresponding author: encarnacion.torralba-penalver@cnrs.fr, stephane.bastide@cnrs.fr

are obtained at significantly lower overpotentials. These are the first results ever reported for PEC-CO_2RR on p-Si photocathodes decorated with AgCu NPs. The proposed deposition method is inexpensive, easily scalable, and can be extended to any bimetallic system whose elements are compatible with MACE of Si.

Keywords: Metal assisted chemical etching (MACE), bimetallic nanoparticles, photo-electroreduction, ratiometric power saved, synergetic effect

1. Introduction

The electrochemical reduction of carbon dioxide (CO_2) into various value-added chemicals and fuels is receiving increasing attention in research and technology. It promises to simultaneous reduce atmospheric CO_2 concentrations and store renewable energy, all by converting CO_2 into useful low carbon products[1]. Among the various existing technologies, the photoelectrochemical CO_2 reduction reaction (PEC-CO_2RR) using semiconductors (SCs) is particularly attractive because it utilizes solar radiation, water and CO_2, that react at the semiconductor/electrolyte interface, somehow mimicking natural photosynthesis[2,3]. The SC acts as a light absorber, for photocarriers generation and collection. Thus, a great deal of effort has been devoted to study the CO_2 reduction using various SCs, such as doped gallium nitride (p-GaN), cadmium telluride (p-CdTe), indium telluride (p-InP), silicon carbide (p-SiC) and silicon (p-Si), among others[4,5].

P-type Si is considered a very good photocathode material due to its optimal energy band gap (~ 1.12 eV) in the visible and near-IR region, its high carrier mobility (on the order of ~10^3 $cm^2\ V^{-1}\ s^{-1}$ at 300 K), its large abundance and the maturity of its processing technologies[6,7]. P-Si photoelectrodes has been decorated with sparsely distributed metal nanoparticles (e.g., Cu, Ag or Au) as catalysts for PEC-CO_2RR. The nanoparticles (NPs) allow the collection of photogenerated charge carriers without preventing light from reaching the semiconductor. Thus, significant photocurrent densities at low overpotentials can be obtained for PEC-CO_2RR due to the catalytic effect of the nanoparticulate metal surface[7,8,9,10]. The catalyst can be preferentially selected from a well-established group of materials leading to identified products[11]: (i) Au, Pd, Ag, and Zn from which carbon monoxide (CO) as the main product; (ii) Pd, Sn, In, and Bi, which produce formate (HCOOH); and (iii) Cu, which can produce hydrocarbons.

Although Cu is known to be the only metal capable of providing hydrocarbons and alcohols in measurable amounts, its selectivity is not optimal. It requires a large overpotential,

and it is ultimately poisoned by CO and byproducts[12,13]. The addition of a second metal to Cu is one of the most promising approaches to improve its selectivity and reactivity[13,14]. Among Cu-based bimetallics, several reports have shown that Ag can significantly activate Cu towards the formation of multi-carbon products[15,16,17]. The faradaic efficiency (FE) and selectivity can be tuned as a function of the AgCu composition and crystalline structure. For example, AgCu nanocrystals with Ag and Cu segregated domains show a 3.4-fold increase in C_2H_4 production at -1.1 V *vs.* RHE (V_{RHE}) with respect to pure Cu[16], or AgCu NWs can reach 72 % FE for CH_4[15].

Despite their interest, very few works have exploited bimetallic nanoelectrocatalysts on p-Si supports for PEC-CO_2RR. In 2016, Kong et al. presented a photocathode based on p-Si Nanowires (SiNWs) decorated with Au_3Cu by drop casting. A CO_2-to-CO FE of 80% was demonstrated at very low overpotentials (-0.2 V_{RHE}) with a photocurrent density of j_{ph} of -5 mA/cm^2 [18]. In 2020, SiNWs decorated with Ni-In were investigated by Ma et al.[19]. A 97% of FE towards HCOOH with a j_{ph} of -7 mA/cm^2 was obtained. With respect to AgCu, in 2019 Gurudayal et al. demonstrated its efficiency integrated at the dark side of p^+nn^+ texturized Si supports, with CO_2 conversion to a mixture of C_2 and C_3 products with 60% FE, at -0.4 V_{RHE} and 10 mA/cm^2. However, this required a high loading of dendritic Cu modified with Ag NPs, which was incompatible with direct illumination of the Si/Metal side[20]. Recently, Cu-Ag thin film catalysts (100 nm in Cu and 3 nm in Ag) were deposited on the illuminated side of p-Si photocathodes[21]. The deposition involved several synthesis and deposition steps including electron beam evaporation, photolithography and lift-off. The photocathodes thus fabricated converted CO_2-to-CO and CO_2-to-CH_4 with a FE of 26.9% and 18.2% at -1.4 and -1.3 V_{RHE}, respectively. The application of a SiO_2 passivation layer further increased the FE at the expense of further increasing the fabrication cost. To the best of our knowledge, the PEC-CO_2RR on p-Si supports decorated with well-dispersed Ag_xCu_{100-x} bimetallic NPs has never been investigated.

The present work reports on the development of a one-step synthesis method of Ag_xCu_{100-x} bimetallic NPs on p-type c-Si by Metal Assisted Chemical Etching (MACE) and their application as photocathodes for PEC-CO_2RR. MACE is a well-established method for the nano- and micro-structuring of Si in hydrofluoric acid (HF) by electroless deposition of single NPs (Ag, Au, Cu, etc.) [22,23]. It does not require any masking or lithography step, it is low cost, simple and easy scalable. Moreover, it has not yet been exploited for bimetallics. The proposed method allows the direct synthesis of Ag_xCu_{100-x} on p-Si in the whole range of atomic compositions. Morphological and compositional analysis performed by SEM-EDX,

XRD and HR-TEM reveal a homogeneous NP distribution, with a phase-separated crystalline structure and a high degree of polycrystallinity, with Ag and Cu homogeneously mixed at the atomic scale. Charge transfer from Cu to Ag in the bimetallic NPs is demonstrated by XPS. The analysis of the PEC-CO_2RR in the as-synthesized materials is performed with $Ag_{50}Cu_{50}$/p-Si, Ag/p-Si, Cu/p-Si and analogous metallic electrodes. A superiority of $Ag_{50}Cu_{50}$/p-Si and Ag/p-Si *vs.* Cu/p-Si is observed under solar illumination, in terms of onset potential, photocurrent density and power saved. Photoelectrolysis coupled to gas chromatography demonstrate the ability of the bimetal to direct selectivity towards high energy density products. A maximum FE for CO and CH_4 of 26 % and 17.8% at -0.75 and -0.86 V_{RHE}, respectively, is obtained. These FEs are very similar to those observed with Cu-Ag thin-film catalysts on p-Si[21], but at a significantly lower overpotential, which add value to the proposed synthesis method. Finally, the effect of long-term photoelectrolysis on the structural stability of the bimetallic is shown. We believe that these findings can contribute to the development of efficient and affordable photoelectrocatalytic materials for solar-assisted CO_2 conversion.

2. Experimental section

2.1. Materials and Reagents

P-type boron doped (100) c-Si polished wafers (ρ = 1-3 ohm cm, thickness ~350±25 μm), purchased from Siegert Wafer were used as substrates for metallization. 30 wt% H_2O_2, 96-97 wt% H_2SO_4, 40 wt% HF, 65 wt% HNO_3 and absolute EtOH (VWR Chemicals) were used as received for Si cleaning. Ag (NO_3) (99.8%) and $Cu(SO_4)\cdot 5H_2O$ (98.5 wt% Cu, Prolabo) were used as a metal salt precursors for the metallization. Dilution and cleaning were performed with 18.2 Mohm cm ultra-pure water (Millipore).

2.2. Photocathode preparation

Si pretreatment: Si wafers were diced into 2x2 cm^2 pieces and cleaned for 20 min in Piranha solution (3:1 v/v H_2SO_4/H_2O_2) to remove organic residues. After extensive rinsing with ultrapure water, the samples were immersed in 1 mol L^{-1} HF for 5 min to remove surface oxides and obtain hydrogen passivation. Polished Ag and Cu plates were used as dark electrodes (section 3.3). Before each electrochemical measurement they were polished with alumina powder (1 and 0.3 μm) and washed thoroughly with ultrapure water. The Cu plate was additionally immersed in HCl/water (50:50 v/v) for oxide removal.

Metal deposition: Metallization of silicon was performed by electroless deposition in HF media (MACE). The pretreated silicon sample was immersed in a HF solution containing a mixture of the salt precursors ($AgNO_3$ and $CuSO_4$) at selected concentrations (see Table 1). The backside of the silicon sample was masked with an adhesive tape to prevent metal deposition on both sides. After MACE, the sample was thoroughly rinsed with water and the adhesive tape was removed. Pure Cu and Ag NPs were synthesized in a similar manner. Different deposition times (from 1 min to 15 min) and HF concentrations (from 0.1 mol L^{-1} to 2.0 M L^{-1}) were tested to investigate the characteristics of the bimetallic Ag_xCu_{100-x} NPs obtained by MACE (see Section 3.1 in Results and Discussion). For the samples used as photocathodes, a HF concentration of 100 mmol L^{-1} and a deposition time of 1 min were chosen. A back contact was formed on the backside of the Si sample by scratching and rubbing In-Ga alloy.

2.3. Physical Characterizations

The morphology and elemental composition (bulk properties) were analyzed by Field Emission Scanning Electron Microscopy (FESEM) coupled with Energy Dispersive X-ray Analysis (SEM-EDX) using a Zeiss Merlin FEG microscope equipped with AZtec EDS Advanced system (HKL Nordlys Nano, Oxford Instruments) and an X-Max SDD detector. Average NP size and surface coverage were determined using ImageJ software. Structural characterization was performed by X-Ray Diffraction (XRD) using a D8 Advanced Bruker diffractometer (Cu Kα radiation). EVA software was used for XRD data processing. Chemical states and surface elemental composition were analyzed by K-alpha X-ray Photoelectron Spectroscopy (XPS) equipped with an ion beam etching from Thermo Fisher Scientific. Microstructural observations were performed by Transmission Electron Microscopy (TEM) with a 200 kV FEG TEM (FEI Tecnai F20 equipped with a Gatan CCD camera Orius 1000, point-to-point resolution 0.24 nm), and the chemical analysis is carried out on the same microscope with an EDX windowless detector (60 mm^2). For TEM observations, NPs were collected on Ni mesh grids by pouring a few drops of ethanol solutions in which the Si/Ag_xCu_{100-x} samples had been previously sonicated.

2.4. Electrochemical measurements

A homemade O-ring type three-electrode photoelectrochemical cell (volume of 54 mL) equipped with a quartz window was used for the electrochemical measurements (see Fig. S1). It was coupled to a Metrohm Autolab PGSTAT 30 potentiostat equipped with NOVA software. The working electrode was the metallized p-Si, the counter electrode was a Pt wire,

and the reference electrode was Ag/AgCl/3 mol L^{-1} KCl (0.209 V *vs*. NHE). All potentials were converted to the RHE reference scale unless otherwise noted (E *vs*. RHE = E *vs*. Ag/AgCl + 0.209 + 0.059 * pH). The electrocatalytic reduction of CO_2 was performed in 0.5 mol L^{-1} $NaHCO_3$ at room temperature (pH = 8.4). Prior to the experiment, 36 mL of electrolyte were added into the cell and purged with Ar for 10 min (pH = 8). The electrolyte was then bubbled with CO_2 (Alphagaz N45) for 20 min to ensure CO_2 saturation (pH ~7.4, $[CO_2]$ = 33 mmol L^{-1}). The CO_2 atmosphere was maintained throughout the experiment. The illuminated silicon surface area was 1.76 cm^2 (O-ring diameter = 15 mm). Cyclic voltammetry was used as the electrochemical characterization technique. The illumination source was a Newport LSH7320 solar simulator providing AM1.5G light with a power of 1000 Wm^{-2}.

2.5. Product analysis

The gas products were analyzed by Gas Chromatography (GC). A Shimadzu gas chromatograph (GC 2010 Pro) equipped with a detector and a Micropacked ShinCarbon GC column was used to analyze the gas composition inside the electrochemical cell during the bulk electrolysis. The gas was sampled from the electrochemical cell and injected into the GC at different electrolysis times. An etalon gas mixture purchased from Air Liquide was used to calculate the concentration of the gases produced. He was used as carrier gas. More details on gas injection and product quantification can be found in the SI.

3. Results and Discussion

3.1. Principle of the bimetallic deposition by MACE

Ag_xCu_{100-x} bimetallic NPs with different compositions were synthesized directly on polished Si substrates by MACE through immersion in a HF solution containing the two ionic metal precursors (Ag^+ and Cu^{2+}, see Experimental section) at different concentrations (Table 1). Several deposition times and HF concentrations were tested to observe their influence on the bimetallic properties. The results are described in the following section.

The principle of the deposition is shown in Fig. 1. As in typical MACE for monometallic deposition, when Ag^+ and/or Cu^{2+} ions get in contact with the Si surface, they are spontaneously reduced by extracting electrons from the Si valence band and deposited on the Si surface as Ag^0 and Cu^0 metal nuclei (Eq. 1). In parallel, Si atoms in the immediate vicinity of the metal ions are oxidized due to hole injection. In HF media, this Si dissolution occurs in the porous silicon formation regime (Eq. 2). The nuclei thus formed become catalytic sites for the subsequent ion reduction and NP growth, with Si atoms close to the NPs providing all the

necessary electrons. The whole process (Eq. 3) is spontaneous, electroless, and provides an optimal metal/p-Si contact without any oxides[24]. One Cu or two Ag atoms can be deposited for each dissolved Si atom (Eq. 4).

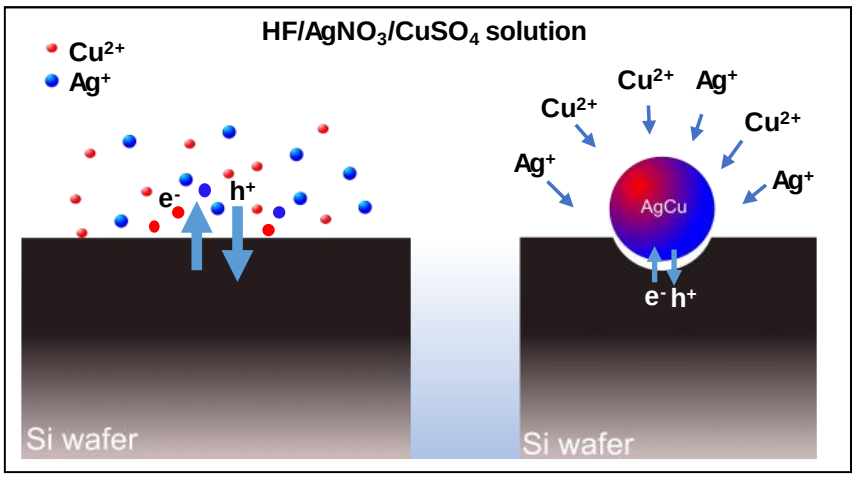

Figure 1: Schematic representation of the electroless synthesis of Ag_xCu_{100-x} bimetallic NPs on Si supports by MACE developed in this work.

Cathodic sites	$M^{n+}_{(aq)} + ne^- \rightarrow M_{(s)}$	M = Ag or Cu; n =1 or 2	Eq. 1
Anodic sites	$Si_{(s)} + 4HF_2^-{}_{(aq)} \rightarrow SiF_6^{2-}{}_{(aq)} + 2e^- + 2HF_{(aq)} + H_{2(g)}$		Eq. 2
Overall reaction	$Si_{(s)} + \frac{2}{n}M^{n+}_{(aq)} + 4HF_2^-{}_{(aq)} \rightarrow \frac{2}{n}M\ (s) + SiF_6^{2-}{}_{(aq)} + 2HF_{(aq)} + H_{2(g)}$		Eq. 3

If Ag^+ and Cu^{2+} are at the same concentration and deposited simultaneously, the overall reaction becomes:

$$Si_{(s)} + (\frac{1}{2}Cu^{2+} + Ag^+)_{(aq)} + 4HF^-_{2(aq)} \rightarrow (\frac{1}{2}Cu + Ag)_{(s)} + SiF^{2-}_{6\ (aq)} + 2HF_{(aq)} + H_{2(g)} \quad \text{Eq. 4}$$

Eq. 4 indicates that there should be 2 times more Cu^{2+} than Ag^+ in the precursor solution (i.e., 2(100-x) moles of Cu^{2+} and x moles of Ag^+) to obtain a given composition Ag_xCu_{100-x}. Its accuracy will be examined below.

3.2. Physicochemical characterization

3.2.1. Surface morphology and atomic composition

The surface morphology of the synthesized Ag, Cu and Ag_xCu_{100-x} NPs have been examined by FESEM as shown in Fig.2. Table 1 shows the molar concentration of the metal precursor solutions and the corresponding atomic composition obtained by EDX together with a plot of the atomic percentage of Cu determined by EDX *vs.* the molar fraction of Cu^{2+} in the precursor solutions (red dots). A solid line indicates the calculated values assuming that, to

obtain a given composition Ag_xCu_{100-x}, there should 2 times more of Cu^{2+} than of Ag^+ in the precursor solution (Eq. 4). The HF concentration for these experiments was 1 mmol L^{-1}.

The EDX data presented in Table 1 reveal that Ag_xCu_{100-x} NPs can be synthesized by our method in the whole range of atomic compositions by simply varying the concentration of metal precursors in the deposition solution. Furthermore, the experimental values for the at. Cu% determined by EDX *vs.* the molar ratio of the metal precursors used overlap very well with the calculated values (solid line), demonstrating the validity of Eq. 4. A clear example is observed for $Ag_{49}Cu_{51}$, where the precursors are in concentrations 1 and 2 mM for Ag^+ and Cu^{2+}, respectively (Table 1). Therefore, the electroless bimetallic deposition of Ag_xCu_{100-x} under these conditions (1 min deposition, 1 mmol L^{-1} HF) on Si supports by MACE is not affected by differences in diffusion coefficients or in reduction kinetics of Ag^+ and Cu^{2+} and obtaining a given composition is straightforward.

Table 1: Molar concentration of the metal precursors used (Ag^+ and Cu^{2+}) and atomic composition of the synthesized Ag_xCu_{100-x} NPs determined by EDX. HF concentration: 1 mmol L^{-1}. Inset: Plot of at% of Cu *vs.* the Cu molar concentration ratio in the precursor solution. (Dots: experimental values. Line: predicted).

Molar Concentration (mmol L^{-1})		**EDX composition (at%)**
Ag^+	**Cu^{2+}**	**Ag_xCu_{100-x}**
1	-	Ag
1	0.5	$Ag_{80}Cu_{20}$
1	1	$Ag_{63}Cu_{37}$
1	2	$Ag_{49}Cu_{51}$
1	3	$Ag_{37}Cu_{63}$
1	4	$Ag_{32}Cu_{68}$
1	5	$Ag_{25}Cu_{75}$
-	1	Cu

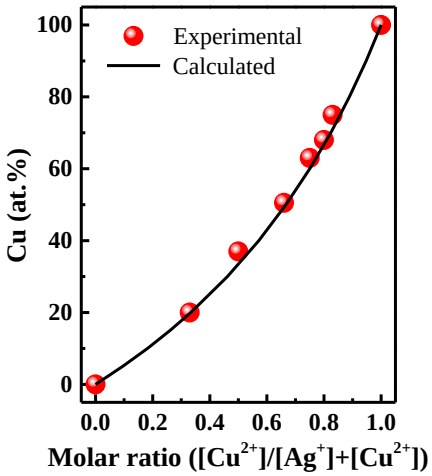

For the sake of simplicity, hereafter we will refer to the averaged atomic composition instead of the exact one if not otherwise stated (e.g. $Ag_{49}Cu_{51}$ will be referred as $Ag_{50}Cu_{50}$ or $Ag_{32}Cu_{68}$ will be referred as $Ag_{30}Cu_{70}$).

The morphology of the deposits is shown in the FESEM images of Fig. 2. Ag NPs are homogeneously distributed on the surface, exhibiting a quasi-spherical shape with an average Feret diameter of 25 nm (Fig. 2(a)) and a surface coverage of ~47%. Pure Cu NPs (Fig. 2(b)) are also quasi-spherical, with an average Feret diameter of 30 nm (similar to Ag NPs) and a

lower surface coverage (~26%). On the other hand, the bimetallic Ag_xCu_{100-x} NPs under these deposition conditions exhibit in general a worm-like elongated shape with several interconnected ligaments in the same NP (clearly observed for a Ag content varying between 20-50 at% (Fig 2(e-h)), with a surface coverage of around 70% and a ligament size of 80 - 90 nm. Interestingly, while the change in morphology from quasi-spherical to worm-like is gradual with decreasing Ag content, it is immediate in the opposite direction (i.e., $Ag_{20}Cu_{80}$ NPs are worm-like shaped while Cu NPs are quasi-spherical).

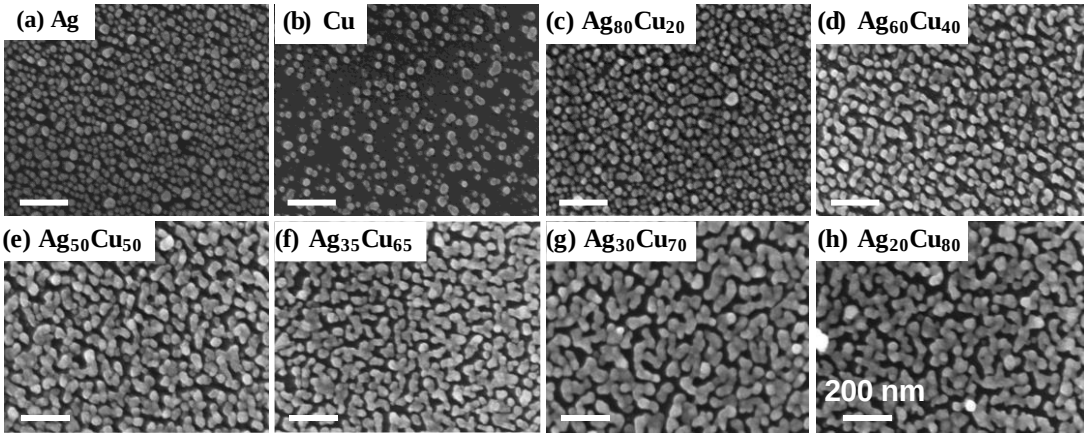

Figure 2: (a-h) Representative FESEM images of Ag_xCu_{100-x} NPs deposited on Si supports by MACE. Averaged atomic composition given on the figures. Deposition time: 1 min at RT, [HF] = 1 mmol L^{-1}.

Fig. S2 shows SEM images comparing $Ag_{50}Cu_{50}$ and $Ag_{20}Cu_{80}$ obtained with a lower concentration of metal ions in the precursor solution with those of Fig. 2. The main difference when we lower the precursor concentration is a notable decrease in the NP size and a modification of the NP morphology from worm-like shaped to quasi-spherical. These experiments show that the more pronounced worm-like morphology of the NPs in Fig. 2 when increasing Cu content is basically due to the higher initial Cu^{2+} concentration (see Table 1), which results in a greater amount of metal deposited. The effect of deposition time and HF concentration on the growth of bimetallic NPs, analyzed by using the $Ag_{50}Cu_{50}$ composition as reference, is shown in the SI (Fig. S3 and S4). The increase of the deposition time highly increases the surface coverage, until a nanoparticulate film is obtained at 5 min deposition (Fig. S3). On the other hand, an elongation of the NP ligaments together with a decrease in surface coverage is observed when increasing the HF concentration (Fig. S4). These experiments exemplify the possibilities of tunning the morphology and the surface coverage of the bimetallic NPs by varying key experimental deposition parameters (precursor concentrations and deposition time).

3.2.2. Crystalline structure and elemental distribution

Fig. 3 (a) shows the X-ray diffraction patterns of Ag, Cu and $Ag_{50}Cu_{50}$ NPs synthesized by electroless deposition on Si. In order to obtain an acceptable signal-to-noise ratio for XRD analysis, the metallization was performed on Si powder instead of flat Si samples. SEM images of the Ag_xCu_{100-x}/p-Si powders are given in the SI (Fig. S5), together with the synthesis details and all data extracted from XRD.

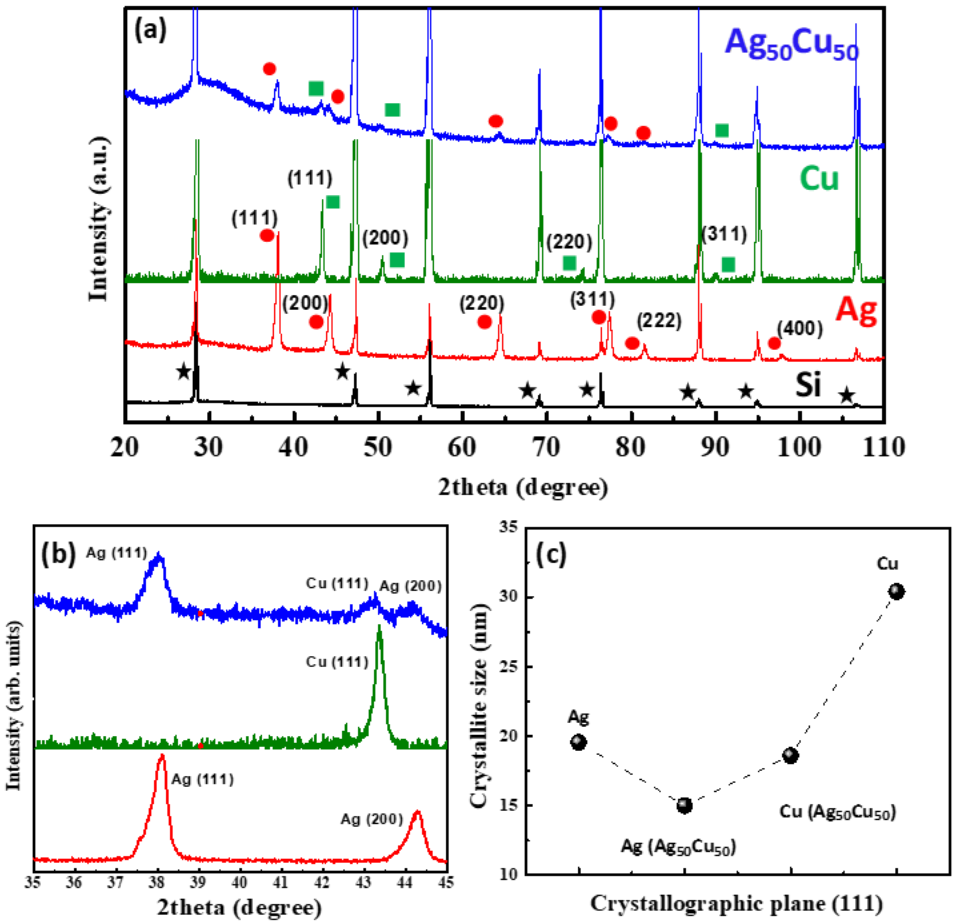

Figure 3: (a) X-ray diffraction patterns of Ag, Cu and $Ag_{50}Cu_{50}$/p-Si powders synthesized by MACE. Squares, circles and stars mark the XRD peaks for Cu, Ag and Si, respectively. (b) Closer view of the XRD patterns focusing on the (111) crystallographic plane; and (c) estimated crystallite sizes of the (111) crystallographic plane for Ag, Cu and $Ag_{50}Cu_{50}$.

The XRD peaks of Ag for Ag/p-Si appear at 2θ values of 39º, 44.5º, 65º,75.8º, 82º and 96.7º and belong to the (111), (200), (220), (311), (222) and (400) crystal planes[25]. The diffractogram of Cu in Cu/p-Si shows a similar pattern, with peaks appearing at 2θ values of 43.5º, 50.7º, 74.14º and 90.2º, corresponding to the (111), (200), (220) and (311) planes[26,27]. The two powders exhibit face-centered cubic (FCC) structures with a polycrystalline nature (broad XRD peaks, see Fig. 3b). The pattern of the synthesized $Ag_{50}Cu_{50}$/p-Si powder

contains the peaks of both pure metals (together with those of the support Si), showing a typical phase-separated crystalline structure[26,28]. These can be the pure Ag and Cu phases or some α (Ag-rich) and β (Cu-rich) phases (fcc α and β solid solutions can reach at high temperature a maximum solubility of 14.1 at% Cu and 4.9 at% Ag, respectively[29]). A closer look at the region of the most intense peaks is shown in Fig. 3 (b). Compared to the (111) peak of pure Ag, that of Ag in $Ag_{50}Cu_{50}$ is not shifted to lower 2θ values, indicating a pure Ag phase in these bimetallics. This is consistent with the fact that Ag and Cu are known to be immiscible in almost all ratios at RT.

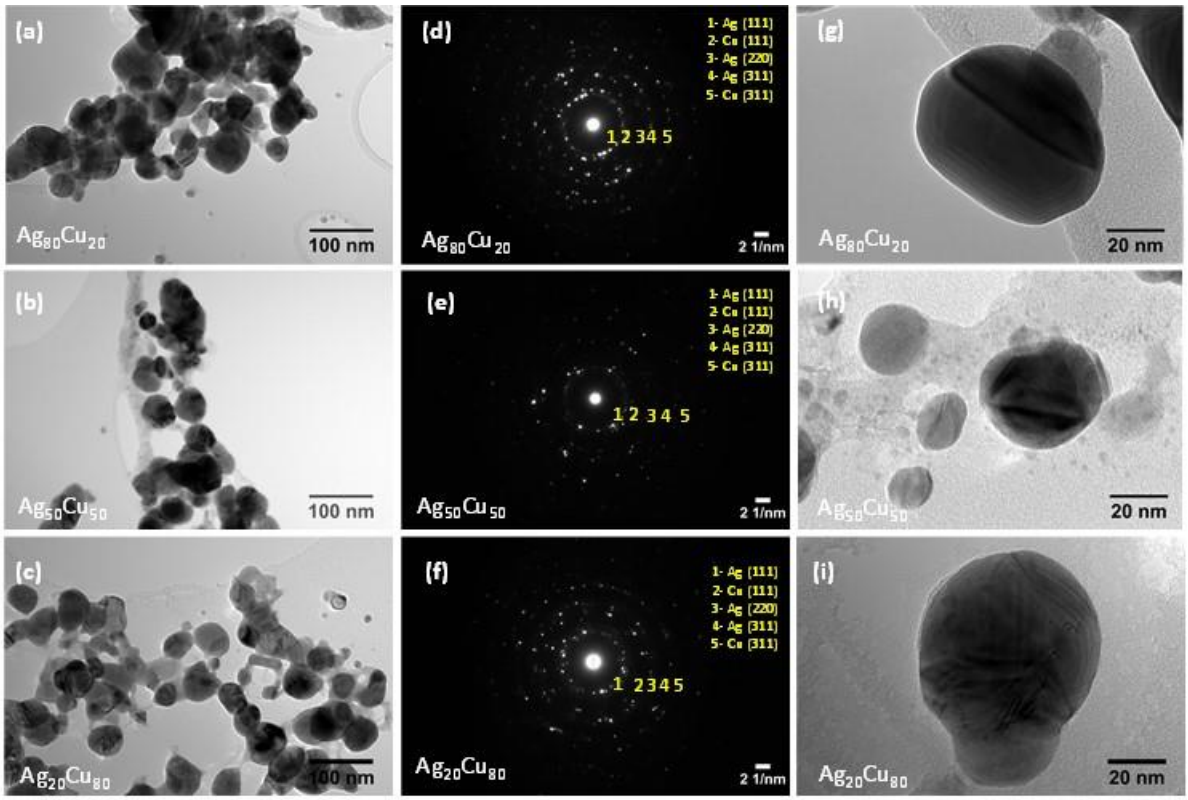

Figure 4: Bright-Field TEM images of the Ag_xCu_{100-x} NPs at low (a)-(c) and high (g)-(i) magnifications. (d)-(f): SAED patterns for the high magnification images and indexed (hkl) planes.

The XRD peaks for the bimetallic are broader than those of pure Ag and Cu, indicating a smaller crystallite size for the bimetallic[30]. Fig. 3(c) shows the crystallite size obtained by applying the Debye-Scherrer formula to the peaks associated to (111) planes (see Table S1 in the Supplementary Information for more details and the values obtained for other crystallographic orientations). The estimated values for Ag and Cu in $Ag_{50}Cu_{50}$ are 15 nm and 19 nm respectively, lower than those of pure metals (c.a. 20 and 30 nm for Ag and Cu crystallites, respectively). Thus, co-depositing Ag and Cu reduces the crystallite size to some extent[28,31].

Further analysis of the structure and bulk composition of the bimetallic NPs was performed by transmission electron microscopy (TEM). Fig. 4 shows HRTEM images of $Ag_{20}Cu_{80}$, $Ag_{50}Cu_{50}$ and $Ag_{80}Cu_{20}$ NPs at low (a-c) and high (g-i) magnification, together with the selected area electron diffraction (SAED) patterns and the indexed (hkl) planes. The *hkl* values were attributed by comparing the *d*-spacing values calculated for the most visible rings (indicated by numbers in the figures) with those obtained by XRD. More details on *d*-spacing calculation from SAED and TEM sample preparation are provided in the SI.

The low magnification TEM images in Fig. 4 (a-c) show typical Ag_xCu_{100-x} NPs agglomerates. The dark and light contrasts that can be observed in some NPs (see also Fig. 4(g-i)) is attributed to moiré patterns, i.e., overlapping of Ag and Cu crystal planes with similar spacing and orientation, as described by Freire et al.[32]. The SAED patterns of Figs. 4(d-f)) show a concentric ring-like structure indicating the polycrystalline nature of the bimetallic NPs. The evaluation of the *d*-spacing values was performed for the most visible rings with the three compositions (results are given in Table S2 of the Supporting Information). The values determined are in very good agreement with those obtained by XRD (Tables S1 and S2). This confirms the presence of both Ag and Cu face-centered crystallites in the NPs, i.e., their phase-separated nature.

To investigate the atomic distribution in the AgCu NPs, high-angle annular dark-field scanning transmission electron microscopy (HAADF-STEM) analysis coupled with EDX mapping was performed on the $Ag_{50}Cu_{50}$ sample (Fig. 5). HAADF-STEM, which is very sensitive to atomic numbers, confirmed the presence of the two different elements in the same NP. The elemental composition of $Ag_{46}Cu_{54}$ is consistent with that obtained from the SEM-EDX data ($Ag_{49}Cu_{51}$, see Table 1). Along with some Cu-rich spots (Fig. 5(c)), the EDX maps of Ag and Cu atoms show a homogeneous distribution of the two elements in the bimetallic NPs (Fig. 5(b-c)), with no apparent distinct phases (Fig. 5(d)). The reason for this is probably the superposition of several Ag and Cu nanocrystallites in the NP volume through which the electron beam passes. Nevertheless, Ag/Cu nanostructures synthesized by soft chemistry routes such as co-reduction or electrodeposition are most often phase segregated (core-shell, crescent, etc.[16,32]). Specific techniques have been developed to synthesize homogeneously dispersed Ag-Cu bimetallic NPs similar to those obtained in this work[15,33].

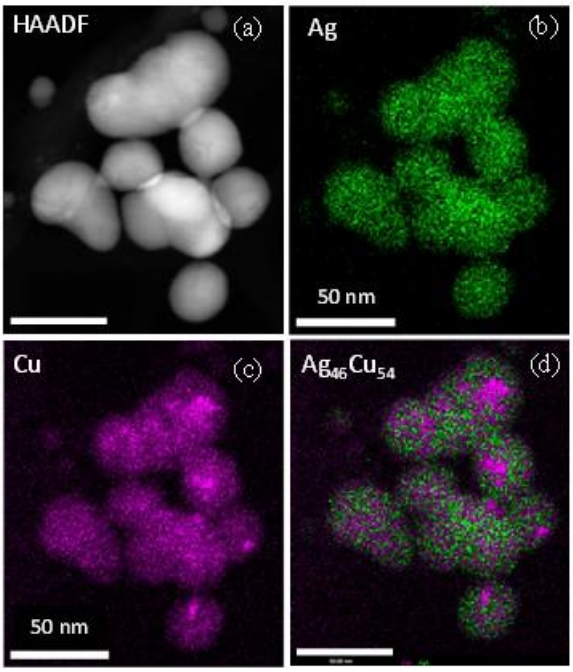

Figure 5: (a) HAADF-STEM image of $Ag_{50}Cu_{50}$ NPs; (b)-(d) EDX elemental mapping in $Ag_{50}Cu_{50}$, Ag (green), Cu (pink).

3.2.3. Chemical state and surface composition

The chemical state and surface composition of the Ag_xCu_{100-x} NPs at different selected compositions were investigated by X-ray photoelectron spectroscopy (XPS). Table 2 summarizes the values measured by XPS and SEM-EDX. The XPS compositional analysis indicates an Ag-rich surface, this characteristic being more pronounced for a bulk Ag content below 50 at%. This difference between bulk and surface compositions can be related to a partial displacement of Cu atoms by Ag^+ ions in solution (given the more noble character of Ag vs. Cu), according to:

$$Cu^0_{(s)} + 2Ag^+_{(aq)} \rightarrow Cu^{2+}_{(aq)} + 2Ag_{(s)} \qquad \text{Eq. 5}$$

This would not affect the bulk composition of the NPs since diffusion of Ag^+ and Cu^{2+} cations is the limiting process during deposition, i.e. there are always enough electrons (from Si oxidation) to reduce them. However, when the deposition is ended, the displacement could affect the surface composition since the Cu atoms eventually displaced can no longer be reduced. Therefore, if Eqs. 1 - 4 correctly describe the essential mechanism of bimetallic deposition by MACE, it must be taken into account that Eq.5 may occur at the NP surface.

Table 2: Atomic compositions of synthesized Ag_xCu_{100-x} NPs determined by XPS and SEM-EDX.

XPS composition (at%)	EDX composition (at%)

$Ag_{89}Cu_{11}$	$Ag_{80}Cu_{20}$
$Ag_{68}Cu_{32}$	$Ag_{63}Cu_{37}$
$Ag_{60}Cu_{40}$	$Ag_{51}Cu_{49}$
$Ag_{53}Cu_{47}$	$Ag_{32}Cu_{68}$
$Ag_{54}Cu_{46}$	$Ag_{25}Cu_{75}$

Fig. 6 shows the core spectra of the Ag *3d* and Cu *2p* emissions for the different samples synthesized (conditions in Table 1). Two well-defined peaks can be observed in the core spectra of Ag *3d* and Cu *2p* for all the compositions (spin doublets $3d_{5/2}$ - $3d_{3/2}$ and $2p_{3/2}$ - $2p_{1/2}$, respectively).

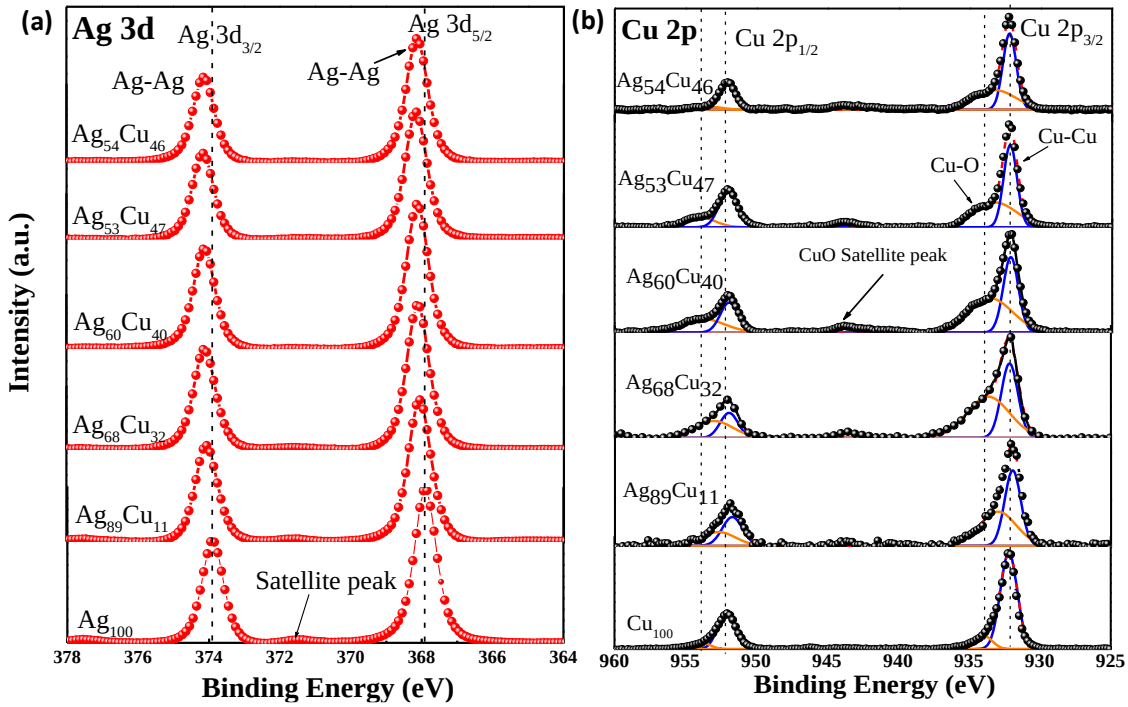

Figure 6: (a) Ag *3d* and (b) Cu *2p* XPS spectra of Ag_xCu_{100-x} NPs deposited on Si by MACE. The peaks in the core spectra of Cu *2p* have been fitted with Cu-Cu and Cu-O contributions (orange and blue lines, respectively). The experimental data recorded are given by red dotted lines for Ag *3d* and black dotted lines for Cu *2p*.

The Ag *3d* peaks for pure Ag NPs (Ag_{100} in the figure) are centered at 367.9 and 373.9 eV. They shift to higher binding energies when the Cu content is increased (e.g., maximum shift of -0.3 eV from Ag_{100} to $Ag_{54}Cu_{46}$, Fig. 6 (a)). The values for Ag-Ag are in good agreement with the bulk values, with little or no oxidized Ag-O observed[34]. The peaks at the Cu *2p* core level are centered at 932.2 eV and 952.1 eV for Cu^0 in pure CuNPs (Cu_{100} in the fig. 6 (b)) A contribution of CuO is also observed at 934.05 eV and 953.9 eV (see Fig. 6 (b)), probably due to native oxide. With increasing Cu content, a small shift of the emission peaks to lower

binding energies is observed (e.g., maximum shift of +0.1 eV from $Ag_{89}Cu_{11}$ to pure Cu). This opposite shift of the binding energies indicates a charge transfer from Cu to Ag upon formation of the bimetallic NPs, i.e., the electron density of Ag atoms is modified by the surrounding Cu atoms and vice-versa in the formed immiscible alloy. Similar observations have already been reported for AgPd alloys[34] or AgCu bimetallic nanodimers with phase-separated structures with improved performance for CO_2RR compared to separated metals[16].

3.3. Photoelectrochemical CO_2RR

3.3.1. Photoelectrochemical *j*/E responses

In order to evaluate the interest of the synthesized Ag_xCu_{100-x}/p-Si as photocathode materials, we first performed the analysis of their j/E response. A simplified schematic representation of the photoelectrochemical cell illustrating the principle of the PEC-CO_2RR measurement is shown in Fig. 7 (a). Briefly, when the Ag_xCu_{100-x}/p-Si photocathode in equilibrium with the electrolyte solution is illuminated with photons of energy equal to or greater than its band gap, $h\nu \geq E_g$ (= 1.12 eV), electrons from the valence band are excited into the conduction band, leaving positive holes behind. Due to the semiconductor band structure, under the application of an external potential, the generated electron/hole pairs are separated and collected; the photo-excited electrons at the photocathode/electrolyte junction to perform the electrochemical reactions (CO_2RR or its competitor hydrogen evolution reaction, HER), and the holes at the back contact of the Si, and from there to the anode to perform the oxygen evolution reaction (OER). More information about PEC and its principles can be found in the reported literature[2,35,36].

Fig. 7 (b) shows the polarization curves (j/E responses) of the different photocathodes under 0.2 sun illumination in CO_2 atmosphere, together with the response of their homologous dark electrodes (i.e., metals used as reference). The j/E response of Ag and Cu was recorded by using Ag and Cu metal plates. $Ag_{50}Cu_{50}/n^{++}$-Si obtained by MACE was used as a dark electrode for $Ag_{50}Cu_{50}$/p-Si (n^{++}-Si, ρ = 3 - 4 mohm cm). The j/E curve of bare p-Si is also shown for reference. Fig. 7(c) shows the power saving analysis for the $Ag_{50}Cu_{50}$/p-Si versus its analogous dark electrode. The table given in Fig. 7(d) presents relevant values to quantify the catalytic activity of the photocathodes extracted from the j/E polarization curves (see figure legend for more details).

All the photocathodes show the typical *j*/E response of a PEC process limited by the photon flux and not by the electrolyte mass transfer (Fig. 7(b)), i.e., the photocurrent, j_{ph}, increases with the applied potential until a j_{ph} plateau is reached when the maximum

photogenerated charge carrier separation and collection is achieved. Similar experiments under stirring did not show an increase in the j_{ph}, confirming that mass transfer in the electrolyte is not a limiting factor. Similarly, the *j*/E responses recorded with increasing illumination power showed a proportional increase in the j_{ph} plateau (Fig. S6(d) in the SI), consistent with this observation. Since the CO_2 concentration in aqueous media is only 33 mM compared to a proton concentration of 1M in the standard state of water, the lack of evidence for mass transport control (e.g., peaks sensitivity to stirring) in the *j*/E signals suggests that CO_2RR and HER occur at similar potentials in our materials, as in most of the studies presented in aqueous systems. A comparison of the j/E responses in Ar and CO_2 confirming this observation is shown in the SI (Fig. S6).

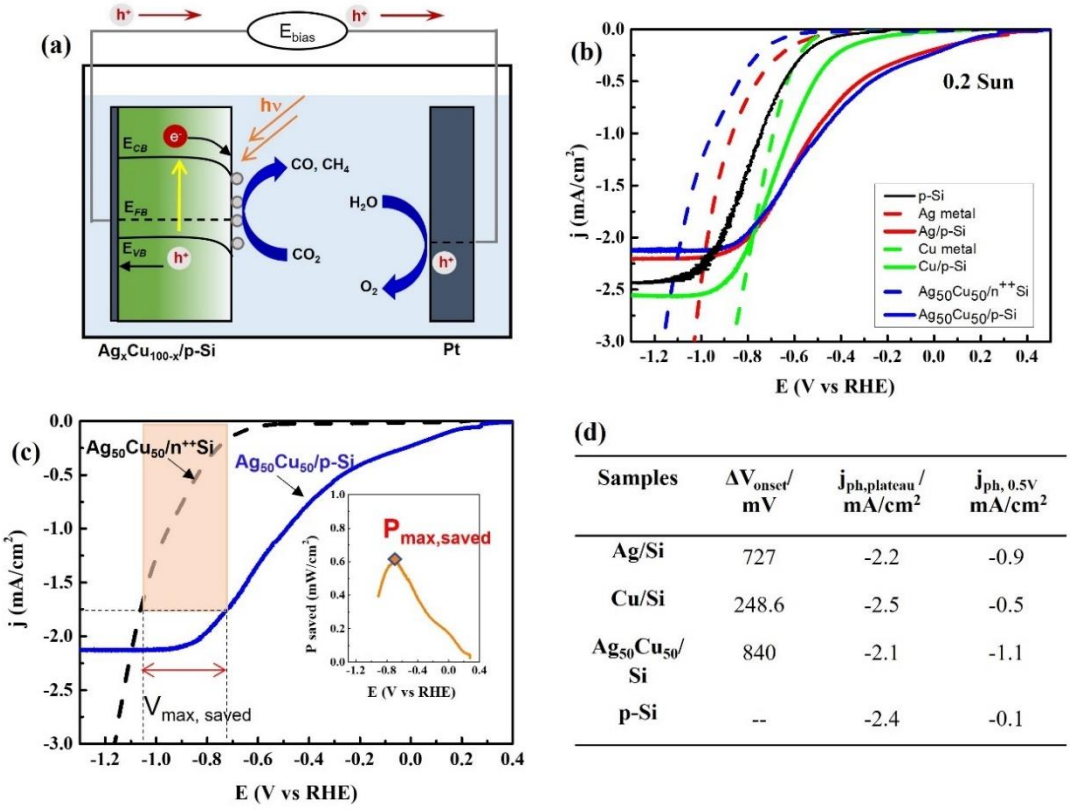

(d)

Samples	ΔV_{onset}/ mV	$j_{ph,plateau}$ / mA/cm²	$j_{ph,\ 0.5V}$ mA/cm²
Ag/Si	727	-2.2	-0.9
Cu/Si	248.6	-2.5	-0.5
$Ag_{50}Cu_{50}$/ Si	840	-2.1	-1.1
p-Si	--	-2.4	-0.1

Figure 7: (a) Scheme of the PEC-CO_2RR using Ag_xCu_{100-x} as photocathode and Pt as anode. (b) Polarization curves of p-Si, Ag/p-Si, Cu/p-Si and $Ag_{50}Cu_{50}$/p-Si under 0.2 sun illumination in CO_2 saturated 0.5 mol L^{-1} $NaHCO_3$, and the corresponding dark electrodes. (c) Blue and black curves: polarization curves of $Ag_{50}Cu_{50}$/p-Si and $Ag_{50}Cu_{50}/n^{++}$-Si (same conditions than in Fig 7b). Inset: power saved (calculated from Eqs. 5) vs. applied potential E for $Ag_{50}Cu_{50}$/p-Si (maximum at ◇). Orange rectangle: actual power saved at *j*/*E* corresponding to $P_{max,saved}$. At this point, $V_{max\ saved}$ = -0.69 V and *j* = -1.67 mA/cm²; (d) ΔV_{onset} (= $E_{onset,\ photocathode}$ -$E_{onset,\ dark\ electrode}$), j_{ph} at the plateau and at 0.5 V_{RHE} (extracted from Fig. 7(b)). E_{onset} is chosen at *j* = -0.1 mA/cm².

The polarization curve of the dark electrodes also shows the typical exponential increase without mass transport limitations. In all cases, the signals appear at significantly more negative potentials than those of the illuminated photocathodes, clearly demonstrating the energy-saving interest of the latter. $Ag_{50}Cu_{50}$/p-Si shows a remarkable ΔV_{onset} of 840 mV, closely followed by Ag/p-Si, with ΔV_{onset} of 727 mV, and Cu/p-Si with 249 mV (*vs* Ag and Cu metals, respectively). The ΔV_{onset} reported here for PEC-CO_2RR with Ag/p-Si and Cu/p-Si photocathodes are in good agreement with those observed in pioneer studies[10]. ΔV_{onset} for a given photocathode is the difference between the onset potential of this photocathode and that of its homologous dark electrode, e.g. $\Delta V_{onset\ p\text{-}Si/AgCu} = E_{onset\ p\text{-}Si/AgCu} - E_{onset\ n^{++}Si/AgCu}$, where E_{onset} is taken for a current density of -0.1 mA cm^{-2} (to avoid the contribution of native metal oxide reduction observed at low cathodic potential). ΔV_{onset} is interesting for power saving metrics, but should not be confused with the photovoltage of a given photocathode, i.e. $|E_{OCP,\ light} - E_{OCP,\ dark}|$, which was close to 40 mV in all cases.

As for the j_{ph} values, the $j_{ph,\ plateau}$ is directly related to the efficiency of the PEC system (catalyst / photoabsorber / electrolyte) to generate and collect photocarriers. We expect $j_{ph,\ plateau}$ to decrease slightly when metal NPs are deposited on the Si surface due to optical losses, since a small fraction of the incident light is reflected by the metal NPs. In our case, j_{ph} is -2.4 mA/cm^2 for bare Si and -2.1 and -2.2 mA/cm^2 for $Ag_{50}Cu_{50}$/p-Si and Ag/p-Si mA/cm^2, respectively, in agreement with the above reasoning. For Cu/p-Si, j_{ph} is slightly higher (-2.6 mA cm^{-2}), which may be due to the low surface coverage of Cu NPs compared to Ag and $Ag_{50}Cu_{50}$.

The j_{ph} values at moderate potentials (-0.5 V_{RHE}) are useful to analyze the catalytic activity. For example, at -0.5 V_{RHE}, a significant current density is obtained for the photocathodes. The highest value is obtained for the $Ag_{50}Cu_{50}$/p-Si (-1.1 mA/cm^2), very close to Ag/p-Si (-0.9 mA/cm^2) and Cu/p-Si (-0.5 mA/cm^2), which is still five times higher than bare Si. These j_{ph} values were recorded at 0.2 sun to avoid distortion of the signal morphology with gas evolution under 1 sun at potentials close to the j_{ph} plateau. Polarization curves at 1 sun are shown in Fig. S6 of the SI. They can reach values as high as 11-12 mA/cm^2, which compares very well with the values reported in the state-of-the-art literature[21].

In order to quantify the energy conversion properties of our materials, we have calculated the ratiometric power saved for the three electrode system (ϕ_{saved}, Fig. 7(c)), as described by Coridan et al.[37]. This figure of merit is defined as the ratio between the power saved at a given

current, P_{saved} (I), by using an illuminated photocathode versus its equivalent dark electrode, and the input solar power, P_{input}:

$$\left.\begin{aligned} \phi_{\text{saved}} &= \frac{\text{P}_{\text{saved}}(\text{I})}{\text{P}_{\text{input}}} * 100 \\ \text{P}_{\text{saved}}(\text{I}) &= \text{I} * \left(\text{E}_{\text{dark}}(\text{I}) - \text{E}_{\text{light}}(\text{I})\right) = \text{I} * \Delta\text{V}_{\text{saved}}(\text{I}) \end{aligned}\right\} \quad \text{Eqs. 5}$$

E_{light} is the potential required to drive the reaction at a selected current value I for the illuminated photocathode and E_{dark} is the corresponding value for the dark electrode. This metric is designed to quantify the performance of individual photoelectrodes and is independent of the potential drops associated with electrochemical processes at the counter-electrode. We refer the reader to Coridan et al.[37] for more details on metrics for energy conversion comparisons in solar fuels and solar electricity generation. ϕ_{saved} is calculated at the maximum saved power, $P_{max,saved}$, as shown in Fig. 7 (c).

The as-calculated ϕ_{saved} for $Ag_{50}Cu_{50}$/p-Si is ~3 %. These values are promising since our photocathodes consist of simple p-Si substrates with a p-Si/electrolyte junction. Future research will be oriented to design Si photocathodes with a buried p-n junction to achieve higher performance (p-n junction Si solar cells typically exhibit a photovoltage of ~700 mV and photovoltaic conversion efficiencies of ~20%). The value obtained with the Ag/p-Si photocathode is also not negligible, ~2.1% (calculation shown in the SI, Fig. S7). For Cu/p-Si, ϕ_{saved} ~ 0.4 %. This does not mean that Cu/p-Si is incapable of converting light into electricity, but its energy conversion performance compared to a Cu metal electrode under the same conditions is very poor. Theoretically, Ag/Si and Cu/Si junctions should have similar rectifying properties (Cu and Ag work functions are 4.64 and 4.70 eV, respectively). The corresponding photocathodes exhibit similar photovoltages (40 mV), indicating that the nature of the Si/metal NPs junction does not significantly affect the electronic properties of the Si(metal NPs)/electrolyte junction. We believe that the poor performance of Cu/Si vs. Ag/Si is more related to the reshaping and loss of Cu during the cathodic scan, resulting in a reduced number of catalytic sites (see also section 3.4.) as compared to Ag which is more stable. Nevertheless, Cu is indispensable for the conversion of CO_2 into carbon products in significant amounts[13]. In the case of AgCu NPs, Ag stabilizes the Cu grains in the bimetallic and prevents these degradation processes for some time.

These results demonstrate the interest of $Ag_{50}Cu_{50}$/p-Si and Ag/p-Si for PEC conversion in terms of onset potentials, j_{ph} and power saved metrics. This superior performance is related to the nanostructuring of the catalyst, which increases the active surface area and multiplies the number of catalytic sites without compromising the photo-

absorber properties, as well as to the intrinsic catalytic properties of the metals. $Ag_{50}Cu_{50}$/p-Si gives slightly higher values than pure Ag, which is undoubtedly related to the electronic and geometric bimetallic effects, as shown in the next section.

3.3.2. Gas products analysis

Electrolysis coupled to gas chromatography (GC) was performed at various applied potentials ranging from -0.37 to -1.07 V_{RHE} for 1h in the CO_2-purged 0.5 M $NaHCO_3$ electrolyte under 1 sun illumination. Fig. 8 shows the current densities and FEs obtained in these measurements. Details of the FE calculations are given in the SI.

Figs 8 (a) and (b) show the chronoamperograms (*j*/t) and the FE values obtained for a $Ag_{50}Cu_{50}$/p-Si photocathode at different potentials. The *j*/t curves are stable with time for low

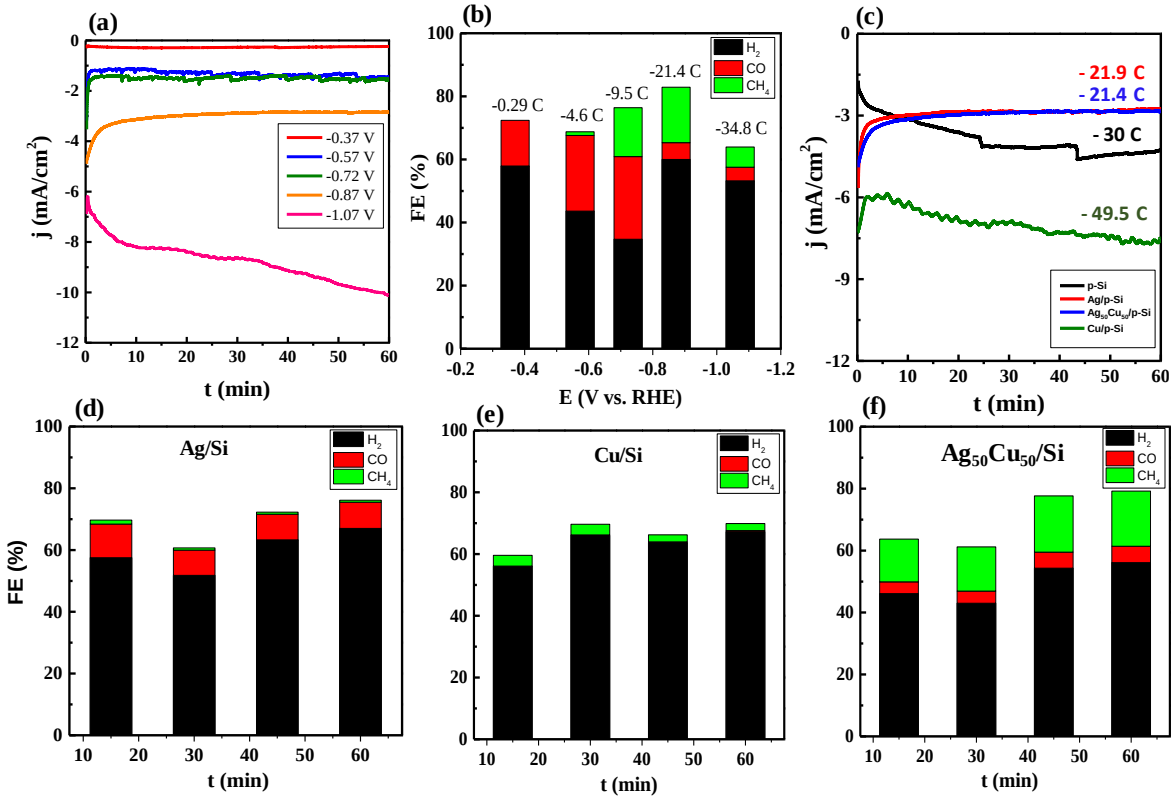

and moderate potentials where relatively little charge crosses the interface (i.e., -0.72 V_{RHE}, 9.5 C passed). From -0.87 V_{RHE} a significant increase in current density is observed and the *j*/t signal begins to increase with time. This behavior is associated with an increase in HER (more details below). The product distribution of the bimetallic photocathode is highly dependent on the applied potential. At low overpotentials, the main CO_2RR product is CO (2 e^- product), with a FE that increases from 14.5% at -0.37 V_{RHE} to a maximum of 26 % at -0.72 V_{RHE}, and then decreases (FE = 4 % at -1.07 V_{RHE}).

Figure 8: (a) j/t responses at different potentials (given on the figure) and (b) FE calculations of $Ag_{50}Cu_{50}$/p-Si in CO_2-purged 0.5 M $NaHCO_3$ electrolyte at 1 Sun illumination; (c) j/t

responses of Ag/p-Si, Cu/p-Si and $Ag_{50}Cu_{50}$/p-Si and p-Si at -0.87 V_{RHE} for 1 h under 1 sun illumination; (d)-(f) the corresponding FE plots.

In addition, CH_4 (8 e^- product) starts to be detected at higher overpotentials (i.e. at -0.57 V_{RHE}) with a FE of 1.1%, reaches a maximum FE of 17.8% at -0.87 V_{RHE} and decreases up to 6% FE at -1.07 V_{RHE}. Thus, the potential range at which CO and CH_4 are produced is well defined and a peak of selectivity for each product is obtained at different potential values. The higher activation energy required for PEC-CO_2RR to CH_4 production *vs.* CO is demonstrated. As for HER, it is dominant at all the applied potentials except -0.72 V_{RHE} (FE_{CO+CH4} = 41.5 % *vs.* FE_{H2} = 35%). At -1.07 V_{RHE}, CH_4 and CO production are strongly suppressed, and HER is enhanced, which coincides with the noticeable increase in current density observed in the j/t curve (Fig. 8a). A decrease in the catalyst coverage during electrolysis, implying more naked Si susceptible to HER, could be at the origin of this phenomena (see next section). The potential -0.87 V_{RHE}, corresponding to the maximum FE_{CH4} (Fig. 8b), was selected for the following experiments.

Fig. 8 (c)-(f) show the *j*/t and FE calculations at -0.87 V_{RHE} for Ag/p-Si, Cu/p-Si and $Ag_{50}Cu_{50}$/p-Si at different electrolysis times. The gas products were analyzed for all the samples every 15 min intervals for 1 h. As can be seen, the Ag/p-Si photocathode produces CO as the main CO_2RR product (with a maximum FE ~10%), and a very small amount of CH_4 (< 1%, Fig. 8(d))[38]. Cu/p-Si produces CH_4, with FE ~3% (Fig.8(e)). In turn, at the selected potential, $Ag_{50}Cu_{50}$/p-Si is able to convert CO_2 into a mixture of CO and CH_4 with a ratio CH_4:CO ~3.75 during the whole electrolysis time, and a maximum of CO_2 conversion at 45 min operation (18.2 % FE for CH_4 and 5.2% for CO, Fig. 8(f)). HER is more important for the photocathodes decorated by monometal than for those with bimetallics, in agreement with their lower CO_2RR performance. In general, the gas product distribution is stable with time, with CO, CH_4 and H_2 being the main products. Equivalent plots for bare Si, Cu and Ag metals are given in the SI (Fig. S8) where H_2 was the only product for bare Si; and Ag and Cu plates produced H_2 and very little CO (FE< 1 % for Ag and FE< 0.5 % for Cu).

Similar results in terms of FEs were recently obtained by Dong. et al.[21], by using a patterned Ag/Cu thin film in a p-Si photocathode fabricated by a multi-step elaboration process (physical deposition, photolithography and lift-off). Under similar experimental conditions, the photocathode converted CO_2 to CO and CO_2 to CH_4 with a maximum FE of 26.9% and 18.2 % at -1.4 and -1.3 V_{RHE}, respectively. Our results are in good agreement with these numbers, with almost identical FEs values but at lower overpotentials (-0.72 and -0.87 V_{RHE} for CO and CH_4, respectively). This shows the interest of bimetallic NP

deposition and gives value to this low-cost and straightforward bimetallic deposition method. Interestingly, Dong et al. greatly improved their FE results by depositing an SiO_2 layer as a mask on bare p-Si, which strongly suppresses HER. This opens up further scope for improving the photocathode efficiencies presented here[21]. It is worth noting that although the present work focuses on the analysis of the gas products (the main products expected according to the literature[21]), preliminary analysis of liquid products by H-NMR have shown up to 5% FE for HCOOH + EtOH for $Ag_{50}Cu_{50}$/p-Si. Table S3 in the supporting information compares our results with FEs reported by other authors.

The results shown in Fig. 8 clearly demonstrate the interest of the bimetallic photocathode to direct the selectivity of the PEC-CO_2RR towards the high energy density product CH_4, and to produce it at moderate overpotentials compared to mono-metal decorated photocathodes and unsupported metals. The enhanced selectivity of the bimetallic towards CH_4 production results from the electronic and geometrical effects generated by the nanoscale coupling of the two metals. This is consistent with the charge transfer from Cu to Ag as evidenced by XPS (Fig.6), confirming a modification of the electronic structure of the bimetallic with an optimized CO* binding energy with respect to the separated metals [16,21], and the high degree of dispersion of Ag and Cu atoms in the bimetallic, as evidenced by XRD and HRTEM (see Figs. 3 and 4), providing an optimum geometry for CO_2-to-CH_4 conversion[15,21].

There seems to be a consensus on the role of Ag and Cu sites in CO_2RR with bimetallic AgCu nanoelectrocatalysts. Ag sites are responsible for the first step (CO_2-to-CO), creating a CO-concentrated environment that Cu sites use to continue the reduction towards C_1 and C_2 products. Once CO is generated, the selectivity between C_1 or C_{2+} products (e.g. CH_4 *vs.* C_2H_4) depends on the bimetallic crystal structure, with AgCu NPs exhibiting segregated domains producing predominantly C_2H_4 (C-C coupling favored on concomitant Cu sites), whereas catalysts with intermixed Ag and Cu domains preferentially produce CH_4. DFT calculations suggest a common pathway for both products with the *COH intermediate, which deviates to CH_4 and C_2H_4 depending on the availability of the catalyst to adsorb H (H_{ad}) or CO (CO_{ad}) and the length scale at which the metal mix favors C-C coupling [15,16,39,40].

3.4. Structural evolution of the catalyst

The chemical state of the catalyst after photoelectrolysis was evaluated by SEM and XPS. Fig. 9 depicts the Cu *2p* core-level emission spectra for the $Ag_{50}Cu_{50}$/p-Si photocathode before and after 1 h of photoelectrolysis (bottom and top rows, respectively), together with representative SEM images.

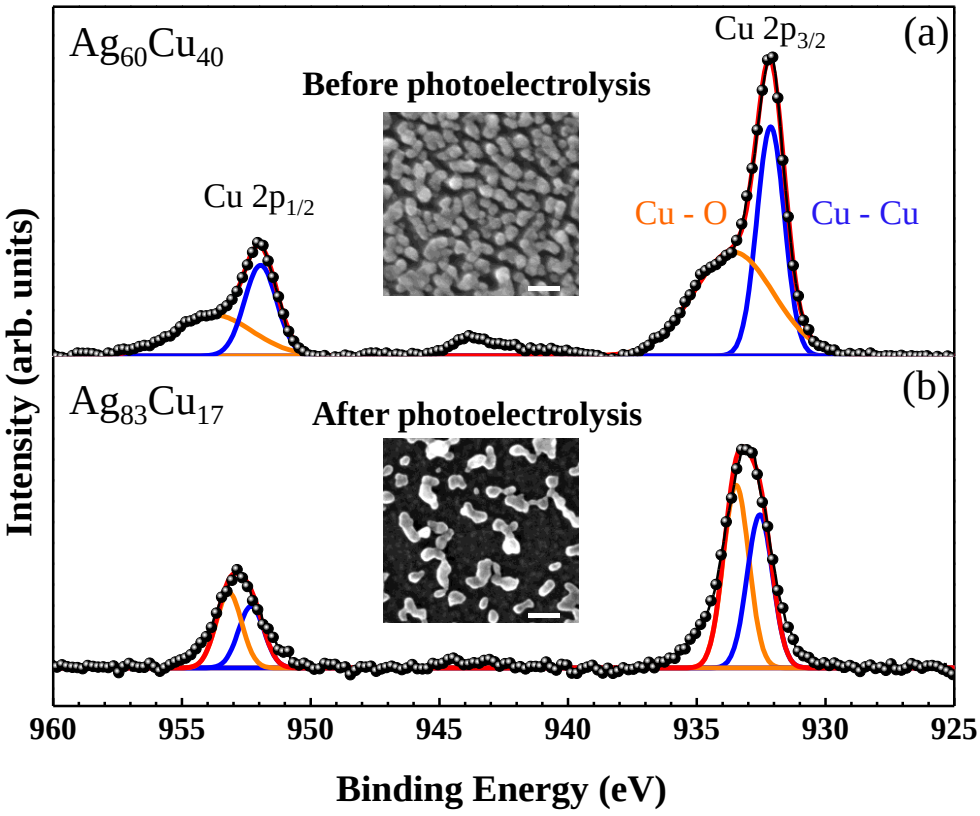

Figure 9: Cu *2p* XPS core-level spectra for (a) $Ag_{50}Cu_{50}$/p-Si before and (b) after 1 h photoelectrolysis at -0.87 V_{RHE}; experimental spectra (black circles) and peak analysis (blue, orange, and red lines). Atomic compositions given on the Figures are the surface compositions measured by XPS. Insets: representative SEM images. The scale bar is 100 nm. Other conditions as in Fig. 6.

SEM-EDX analysis revealed a decrease in NP coverage and a loss of Cu after photoelectrolysis. Specifically, the surface composition changed from $Ag_{60}Cu_{40}$ to $Ag_{83}Cu_{17}$, as determined by XPS. A significant amount of oxidized Cu was observed on the surface after photoelectrolysis (probably due to a longer air exposure after this experiment). Fig. S9 in the SI shows the XPS analysis of an $Ag_{50}Cu_{50}$/p-Si photocathode after 3 h of photoelectrolysis under the same conditions. An atomic surface composition of $Ag_{92}Cu_8$ was measured by XPS, confirming a further loss of Cu during prolonged electrolysis. A detachment of Ag nanograins could not be observed after 1 h, but has been reported for long electrolysis times (24 h) [41].

The instability of Cu catalysts during CO_2RR is well known. Nanoscale degradation mechanisms in Cu surfaces during CO_2RR include detachment, dissolution, reshaping, fragmentation and agglomeration [42,43]. For example, in recent works on PEC-CO_2RR with Cu NPs/p-Si photocathodes, the poor adhesion of Cu to Si has been pointed out as a possible reason for catalysts degradation[9]. Two main factors are thought to be responsible: (i) structural reorganization of the catalysts under the application of a potential and (ii) CO adsorption on

Cu sites leading to Cu coordination and detachment[43,44]. In the specific case of CO_2RR on Ag-Cu core-sell NPs, the latter has been identified as the main cause of instability [43]. It is possible that a similar phenomenon occurs in our bimetallic photocathode, although the crystalline structure is not identical. Recently, P. Yang et al. have reported a study of the evolution of dimeric and intermixed AgCu on carbon supports during CO_2RR[39]. They showed that, regardless of the initial catalyst structure, Cu can move and leach out of the catalysts to be detached/re-deposited elsewhere, which is consistent with our observations[39,44]. Systematic studies of catalyst degradation as a function of time and composition are underway in our laboratory. The addition of atomic-scale protective layers (TiO_2, SiO_2, Al_2O_3) or the anchoring of NPs to the photoelectrode[45] are being implemented to increase the stability of these systems.

4. Conclusion

We have developed an innovative method for the deposition of Ag_xCu_{100-x} bimetallic NPs on Si by MACE. It allows to control the bimetallic composition and to tune the NP morphology (from quasi-spherical to elongated worm-like structures) and the surface coverage using key experimental parameters. XRD, SAED and HAADF-STEM patterns show a phase-separated polycrystalline structure with highly dispersed Ag and Cu nanocrystallites (~15 nm), which is quite unusual for soft-chemistry synthesized AgCu NPs. XPS compositional analysis shows Ag-rich surfaces. Opposite shifts in the binding energies of the Cu 2p and Ag 3d core signals with atomic composition indicate a charge transfer from Cu to Ag in the bimetallics.

The performance of the as-synthesized Ag_xCu_{100-x}/p-Si materials as photocathodes for PEC-CO_2RR has been evaluated by analyzing their polarization curves and of product distribution. A better performance of $Ag_{50}Cu_{50}$/p-Si and Ag/p-Si *vs.* Cu/p-Si under solar illumination is observed compared to the corresponding dark electrodes ($Ag_{50}Cu_{50}$/n^{++}-Si and Ag metal, respectively) in terms of onset potentials, photocurrent densities and power saving metrics. In particular, a remarkable positive potential shift of ~ 840 mV *vs.* $Ag_{50}Cu_{50}$/n^{++}Si and a ratiometric power saved of ~ 3% have been obtained for $Ag_{50}Cu_{50}$/p-Si. Finally, photoelectrolysis coupled to gas chromatography has been performed at different potentials and electrolysis times. Maximum FEs for CO and CH_4 of 26 % and 17.8% at -0.75 and -0.86 VRHE, respectively, have been obtained. These FEs compare favorably with those reported in the recent literature. The study demonstrates the ability of the bimetallic photocathode to guide the selectivity of PEC-CO_2RR towards high energy density products (i.e., CH_4) with

respect to the monometal-decorated homologue. The specific electronic and geometric properties, as evidenced by XPS and HRTEM, account for this bimetallic effect. Our study demonstrates the interest of bimetallic deposition by MACE and its potential impact on the rapid and cost-effective preparation of Cu-based bimetallic Si photocathodes for efficient PEC-CO_2RR.

Conflict of interest

There is no conflict of interest between the authors.

Associated content

Supporting Information: (1) Experimental setup displaying the O-ring type three-electrode photoelectrochemical cell; (2) FESEM images showing the effect of the metal precursor concentration, deposition time and HF concentration on the morphology of the bimetallic deposits; (3) synthesis of Ag/p-Si, Cu/p-Si and $Ag_{50}Cu_{50}$ powders for XRD analysis and crystallite size and *d*-spacing calculations from XRD; (4) TEM samples preparation and d-spacing calculation from SAED, (5) Comparison of the j/E signals at different illumination power (0.2 Sun, 0.5 Sun and 1 Sun) and gas atmospheres (Ar and CO_2), power conversion efficiency calculation for Ag/p-Si and Cu/p-Si *vs* metal electrodes, FE measurements for bare Si, Ag metal and Cu metal electrodes and FE comparison table with values from other authors, (6) XPS after 3 hours photoelectrolysis.

Author information

Corresponding Author:

Encarnacion Torralba- Univ Paris Est Creteil, CNRS, ICMPE, UMR 7182, 2 rue Henri Dunant, 94320 Thiais, France **Email id:** encarnacion.torralba-penalver@cnrs.fr

Stephane Bastide - Univ Paris Est Creteil, CNRS, ICMPE, UMR 7182, 2 rue Henri Dunant, 94320 Thiais, France **Email id:** stephane.bastide@cnrs.fr

Authors

Harsh A. Chaliyawala- Univ Paris Est Creteil, CNRS, ICMPE, UMR 7182, 2 rue Henri Dunant, 94320 Thiais, France.

Diane Muller-Bouvet- Univ Paris Est Creteil, CNRS, ICMPE, UMR 7182, 2 rue Henri Dunant, 94320 Thiais, France

Christophe Pichon- Univ Paris Est Creteil, CNRS, ICMPE, UMR 7182, 2 rue Henri Dunant, 94320 Thiais, France

Kadiatou Bah- Univ Paris Est Creteil, CNRS, ICMPE, UMR 7182, 2 rue Henri Dunant, 94320 Thiais, France

Anffane Djoumoi- Univ Paris Est Creteil, CNRS, ICMPE, UMR 7182, 2 rue Henri Dunant, 94320 Thiais, France

Frédéric Marty- ESYCOM - Electronique, Systèmes de communication et Microsystèmes (Université de Paris-Est - Marne-la-Vallée) Cité Descartes, 77454 Marne-la-Vallée Cedex 2, France

Tarik Bourouina- ESYCOM - Electronique, Systèmes de communication et Microsystèmes (Université de Paris-Est - Marne-la-Vallée) Cité Descartes, 77454 Marne-la-Vallée Cedex 2, France

Author contribution

H. Chaliyawala performed the body of experimental work and contributed to the writing. S. Bastide contributed to the conception of the experiments, writing and supervision. D. M-Bouvet performed the XRD characterizations. C. Pichon performed the NMR measurements. K. Bah performed the XPS measurements. A. Djoumoi. contributed to the experimental work. F. Marty and T. Bourouina contributed to the conception of the study, E.T. contributed to the conception, writing and supervision.

Funding Sources

French National Research Agency (ANR JCJC SIROCCO 2022-2024), I-Site Project Future (Exploratory project EVOLVE 2021-2022, Gustave Eiffel University).

Acknowledgment

This work was supported by the French National Research Agency (ANR JCJC SIROCCO 2022-2024) and the I-Site Project Future (Exploratory project EVOLVE 2021-2022, Gustave Eiffel University). H. Chaliyawala acknowledges Paris-East Creteil University (UPEC) for a postdoctoral fellowship (2020-2021). The authors also acknowledge Dr. S. Le Gall from the Electrical Engineering Group of Paris (GeePs), Paris-Saclay University, for fruitful discussions on bimetallic electronic properties, J. Bourgon for HRTEM, SAED and HAADF-STEM studies, and R. Pires Brazuna for technical assistance with the SEM/EDX instrument (Microscopy facilities of the East-Paris Institute of Chemistry and Materials). Finally, the authors acknowledge the support of the Centre National de la Recherche Scientifique (CNRS) for providing the central facilities to carry out this work.

References

(1) Durst, J.; Rudnev, A.; Dutta, A.; Fu, Y.; Herranz, J.; Kaliginedi, V.; Kuzume, A.; Permyakova, A. A.; Paratcha, Y.; Broekmann, P.; Schmidt, T. J. Electrochemical CO_2 Reduction -A Critical View on Fundamentals, Materials and Applications. *Chimia* **2015**, *69* (12), 769–776. https://doi.org/10.2533/chimia.2015.769.

(2) He, J.; Janáky, C. Recent Advances in Solar-Driven Carbon Dioxide Conversion: Expectations versus Reality. *ACS Energy Letters* **2020**, *5* (6), 1996–2014. https://doi.org/10.1021/acsenergylett.0c00645.

(3) Kan, M.; Wang, Q.; Hao, S.; Guan, A.; Chen, Y.; Zhang, Q.; Han, Q.; Zheng, G. System Engineering Enhances Photoelectrochemical CO2Reduction. *Journal of Physical Chemistry C* **2022**, *126* (4), 1689–1700. https://doi.org/10.1021/acs.jpcc.1c10156.

(4) Kumaravel, V.; Bartlett, J.; Pillai, S. C. Photoelectrochemical Conversion of Carbon Dioxide (CO_2) into Fuels and Value-Added Products. *ACS Energy Letters* **2020**, 486–519. https://doi.org/10.1021/acsenergylett.9b02585.

(5) Kim, J.; Kwon, E. E. Photoconversion of Carbon Dioxide into Fuels Using Semiconductors. *Journal of CO_2 Utilization* **2019**, *33* (April), 72–82. https://doi.org/10.1016/j.jcou.2019.05.012.

(6) Yalamanchili, S.; Kempler, P. A.; Papadantonakis, K. M.; Atwater, H. A.; Lewis, N. S. Integration of Electrocatalysts with Silicon Microcone Arrays for Minimization of Optical and Overpotential Losses during Sunlight-Driven Hydrogen Evolution. *Sustainable Energy and Fuels* **2019**, *3* (9), 2217–2236. https://doi.org/10.1039/c9se00294d.

(7) Kempler, P. A.; Richter, M. H.; Cheng, W. H.; Brunschwig, B. S.; Lewis, N. S. Si Microwire-Array Photocathodes Decorated with Cu Allow CO_2 Reduction with Minimal Parasitic Absorption of Sunlight. *ACS Energy Letters* **2020**, *5* (8), 2528–2534. https://doi.org/10.1021/acsenergylett.0c01334.

(8) Hinogami, R.; Nakamura, Y.; Yae, S.; Nakato, Y. An Approach to Ideal Semiconductor Electrodes for Efficient Photoelectrochemical Reduction of Carbon Dioxide by Modification with Small Metal Particles. *The Journal of Physical Chemistry B* **2002**, *102* (6), 974–980. https://doi.org/10.1021/jp972663h.

(9) Roh, I.; Yu, S.; Lin, C. K.; Louisia, S.; Cestellos-Blanco, S.; Yang, P. Photoelectrochemical CO_2 Reduction toward Multicarbon Products with Silicon Nanowire Photocathodes Interfaced with Copper Nanoparticles. *Journal of the American Chemical Society* **2022**. https://doi.org/10.1021/jacs.2c03702.

(10) Hinogami, R.; Nakamura, Y.; Yae, S.; Nakato, Y. Modification of Semiconductor Surface with Ultrafine Metal Particles for Efficient Photoelectrochemical Reduction of Carbon Dioxide. *Applied Surface Science* **1997**, *121–122*, 301–304. https://doi.org/10.1016/S0169-4332(97)00310-3.

(11) Zhang, W.; Hu, Y.; Ma, L.; Zhu, G.; Wang, Y.; Xue, X.; Chen, R.; Yang, S.; Jin, Z. Progress and Perspective of Electrocatalytic CO_2 Reduction for Renewable Carbonaceous Fuels and Chemicals. *Advanced Science* **2018**, *5* (1). https://doi.org/10.1002/advs.201700275.

(12) Wang, K.; Ma, Y.; Liu, Y.; Qiu, W.; Wang, Q.; Yang, X.; Liu, M.; Qiu, X.; Li, W.; Li, J. Insights into the Development of Cu-Based Photocathodes for Carbon Dioxide (CO_2) Conversion. *Green Chemistry* **2021**, *23* (9), 3207–3240. https://doi.org/10.1039/d0gc04417b.

(13) Lee, C. W.; Yang, K. D.; Nam, D. H.; Jang, J. H.; Cho, N. H.; Im, S. W.; Nam, K. T. Defining a Materials Database for the Design of Copper Binary Alloy Catalysts for Electrochemical CO_2 Conversion. *Advanced Materials* **2018**, *30* (42), 1–18. https://doi.org/10.1002/adma.201704717.

(14) Zhu, W.; Tackett, B. M.; Chen, J. G.; Jiao, F. Bimetallic Electrocatalysts for CO_2 Reduction. *Topics in Current Chemistry* **2018**, *376* (6), 1–21. https://doi.org/10.1007/s41061-018-0220-5.

(15) Choi, C.; Cai, J.; Lee, C.; Lee, H. M.; Xu, M.; Huang, Y. Intimate Atomic Cu-Ag Interfaces for High CO_2RR Selectivity towards CH_4 at Low over Potential. *Nano Research* **2021**, *14* (10), 3497–3501. https://doi.org/10.1007/s12274-021-3639-x.

(16) Huang, J.; Mensi, M.; Oveisi, E.; Mantella, V.; Buonsanti, R. Structural Sensitivities in Bimetallic Catalysts for Electrochemical CO2 Reduction Revealed by Ag-Cu Nanodimers. *Journal of the American Chemical Society* **2019**, *141* (6), 2490–2499. https://doi.org/10.1021/jacs.8b12381.

(17) Lee, S.; Park, G.; Lee, J. Importance of Ag-Cu Biphasic Boundaries for Selective Electrochemical Reduction of CO_2 to Ethanol. *ACS Catalysis* **2017**, *7* (12), 8594–8604. https://doi.org/10.1021/acscatal.7b02822.

(18) Kong, Q.; Kim, D.; Liu, C.; Yu, Y.; Su, Y.; Li, Y.; Yang, P. Directed Assembly of Nanoparticle Catalysts on Nanowire Photoelectrodes for Photoelectrochemical CO_2 Reduction. *Nano Letters* **2016**, *16* (9), 5675–5680. https://doi.org/10.1021/acs.nanolett.6b02321.

(19) Ma, W.; Xie, M.; Xie, S.; Wei, L.; Cai, Y.; Zhang, Q.; Wang, Y. Nickel and Indium Core-Shell Co-Catalysts Loaded Silicon Nanowire Arrays for Efficient Photoelectrocatalytic Reduction of CO_2 to Formate. *Journal of Energy Chemistry* **2021**, *54*, 422–428. https://doi.org/10.1016/j.jechem.2020.06.023.

(20) Gurudayal; Beeman, J. W.; Bullock, J.; Wang, H.; Eichhorn, J.; Towle, C.; Javey, A.; Toma, F. M.; Mathews, N.; Ager, J. W. Si Photocathode with Ag-Supported Dendritic Cu Catalyst for CO_2 Reduction. *Energy and Environmental Science* **2019**, *12* (3), 1068–1077. https://doi.org/10.1039/c8ee03547d.

(21) Dong, W. J.; Lim, J. W.; Hong, D. M.; Kim, J.; Park, J. Y.; Cho, W. S.; Baek, S.; Lee, J.-L. Grain Boundary Engineering of Cu–Ag Thin-Film Catalysts for Selective (Photo)Electrochemical CO_2 Reduction to CO and CH_4. *ACS Appl. Mater. Interfaces* **2021**, *13* (16), 18905–18913. https://doi.org/10.1021/acsami.1c03735.

(22) Yae, S.; Nasu, N.; Matsumoto, K.; Hagihara, T.; Fukumuro, N.; Matsuda, H. Nucleation Behavior in Electroless Displacement Deposition of Metals on Silicon from Hydrofluoric Acid Solutions. *Electrochimica Acta* **2007**, *53* (1), 35–41. https://doi.org/10.1016/j.electacta.2007.04.058.

(23) Torralba, E.; Le Gall, S.; Lachaume, R.; Magnin, V.; Harari, J.; Halbwax, M.; Vilcot, J.-P.; Cachet-Vivier, C.; Bastide, S. Tunable Surface Structuration of Silicon by Metal Assisted Chemical Etching with Pt Nanoparticles under Electrochemical Bias. *ACS Appl. Mater. Interfaces* **2016**, *8* (45), 31375–31384. https://doi.org/10.1021/acsami.6b09036.

(24) Chartier, C.; Bastide, S.; Lévy-Clément, C. Metal-Assisted Chemical Etching of Silicon in HF-H_2O_2. *Electrochimica Acta* **2008**, *53* (17), 5509–5516. https://doi.org/10.1016/j.electacta.2008.03.009.

(25) Khan, M. A. M.; Kumar, S.; Ahamed, M.; Alrokayan, S. A.; AlSalhi, M. S. Structural and Thermal Studies of Silver Nanoparticles and Electrical Transport Study of Their Thin Films. *Nanoscale Research Letters* **2011**, *6*, 1–8. https://doi.org/10.1186/1556-276X-6-434.

(26) Lin, H. K.; Huang, C. W.; Lin, Y. H.; Chuang, W. S.; Huang, J. C. Effects of Accumulated Energy on Nanoparticle Formation in Pulsed-Laser Dewetting of AgCu Thin Films. *Nanoscale Research Letters* **2021**, *16* (1). https://doi.org/10.1186/s11671-021-03564-5.

(27) Dutta, A.; Montiel, I. Z.; Erni, R.; Kiran, K.; Rahaman, M.; Drnec, J.; Broekmann, P. Activation of Bimetallic AgCu Foam Electrocatalysts for Ethanol Formation from CO_2

by Selective Cu Oxidation/Reduction. *Nano Energy* **2020**, *68*, 104331. https://doi.org/10.1016/j.nanoen.2019.104331.

(28) Kushchev, S. B.; Bosykh, M. A.; Kannykin, S. V.; Kostyuchenko, A. V.; Soldatenko, S. A.; Antonova, M. S. Structure and Mechanical Properties of Ag-Cu Films Prepared by Vacuum Codeposition of Au and Cu. *Inorganic Materials* **2015**, *51* (7), 673–678. https://doi.org/10.1134/S0020168515070092.

(29) Subramanian, P. R.; Perepezko, J. H. The Ag-Cu (Silver-Copper) System. *JPE* **1993**, *14* (1), 62–75. https://doi.org/10.1007/BF02652162.

(30) Torralba, E.; Blanchard, N.; Cachet-Vivier, C.; Muller-Bouvet, D.; González, J.; Bastide, S. Electrochemical Study of Carbon Dioxide Reduction at Copper–Palladium Nanoparticles: Influence of the Bimetallic Composition in the CO Poisoning Tolerance. *Electrochimica Acta* **2020**, *354*, 0–10. https://doi.org/10.1016/j.electacta.2020.136739.

(31) Loza, K.; Heggen, M.; Epple, M. Synthesis, Structure, Properties, and Applications of Bimetallic Nanoparticles of Noble Metals. *Advanced Functional Materials* **2020**, *30* (21). https://doi.org/10.1002/adfm.201909260.

(32) Freire, R. M.; Rojas-Nunez, J.; Elias-Arriaga, A. L.; Fujisawa, K.; Troncoso, L.; Denardin, J. C.; Baltazar, S. E. Natural Arrangement of AgCu Bimetallic Nanostructures through Oleylamine Reduction. *Inorganic Chemistry Frontiers* **2020**, *7* (24), 4902–4912. https://doi.org/10.1039/d0qi00940g.

(33) Yang, C.; Ko, B. H.; Hwang, S.; Liu, Z.; Yao, Y.; Luc, W.; Cui, M.; Malkani, A. S.; Li, T.; Wang, X.; Dai, J.; Xu, B.; Wang, G.; Su, D.; Jiao, F.; Hu, L. Overcoming Immiscibility toward Bimetallic Catalyst Library. *Science Advances* **2020**, *6* (17), 1–10. https://doi.org/10.1126/sciadv.aaz6844.

(34) Sengar, S. K.; Mehta, B. R.; Govind. Size and Alloying Induced Shift in Core and Valence Bands of Pd-Ag and Pd-Cu Nanoparticles. *Journal of Applied Physics* **2014**, *115* (12). https://doi.org/10.1063/1.4869437.

(35) Allen J. Bard, Martin Stratmann, Fritz Scholz, C. J. P. *Encyclopedia of Electrochemistry: Inorganic Electrochemistry*; 2006. https://doi.org/10.1002/9783527610426.bard060001.

(36) Ming X. Tan, Paul E Laibinis, Sonbinh T. Nguyen, Janet M. Kesselman, Colby E. Stanton, N. S. L. *Principles and Applications of Semiconductor Photoelectrochemistry*; Wiley, 1994. https://doi.org/10.1002/9780470166420.ch2.

(37) Coridan, R. H.; Nielander, A. C.; Francis, S. A.; McDowell, M. T.; Dix, V.; Chatman, S. M.; Lewis, N. S. Methods for Comparing the Performance of Energy-Conversion

Systems for Use in Solar Fuels and Solar Electricity Generation. *Energy and Environmental Science* **2015**, *8* (10), 2886–2901. https://doi.org/10.1039/c5ee00777a.

(38) Kuhl, K. P.; Hatsukade, T.; Cave, E. R.; Abram, D. N.; Kibsgaard, J.; Jaramillo, T. F. Electrocatalytic Conversion of Carbon Dioxide to Methane and Methanol on Transition Metal Surfaces. *Journal of the American Chemical Society* **2014**, *136* (40), 14107–14113. https://doi.org/10.1021/ja505791r.

(39) Chen, P.-C.; Chen, C.; Yang, Y.; Maulana, A. L.; Jin, J.; Feijoo, J.; Yang, P. Chemical and Structural Evolution of AgCu Catalysts in Electrochemical CO $_2$ Reduction. *J. Am. Chem. Soc.* **2023**, *145* (18), 10116–10125. https://doi.org/10.1021/jacs.3c00467.

(40) Gao, J.; Zhang, H.; Guo, X.; Luo, J.; Zakeeruddin, S. M.; Ren, D.; Grätzel, M. Selective C–C Coupling in Carbon Dioxide Electroreduction via Efficient Spillover of Intermediates As Supported by Operando Raman Spectroscopy. *J. Am. Chem. Soc.* **2019**, *141* (47), 18704–18714. https://doi.org/10.1021/jacs.9b07415.

(41) Yu, J.; Zhang, H.; Cai, T.; Wang, W.; Mu, L.; She, G.; Shi, W. Silver Nanoparticles Embedded within a Silicon Photocathode for Photoelectrochemical Fixation of CO_2 to Synthesize Intermediates of Profen Drugs. *ACS Appl. Nano Mater.* **2023**, *6* (2), 821–826. https://doi.org/10.1021/acsanm.2c04810.

(42) Popović, S.; Smiljanić, M.; Jovanovič, P.; Vavra, J.; Buonsanti, R.; Hodnik, N. Stability and Degradation Mechanisms of Copper-Based Catalysts for Electrochemical CO2 Reduction. *Angewandte Chemie - International Edition* **2020**, *59* (35), 14736–14746. https://doi.org/10.1002/anie.202000617.

(43) Wilde, P.; O'Mara, P. B.; Junqueira, J. R. C.; Tarnev, T.; Benedetti, T. M.; Andronescu, C.; Chen, Y. T.; Tilley, R. D.; Schuhmann, W.; Gooding, J. J. Is Cu Instability during the CO2reduction Reaction Governed by the Applied Potential or the Local CO Concentration? *Chemical Science* **2021**, *12* (11), 4028–4033. https://doi.org/10.1039/d0sc05990k.

(44) Yang, Y.; Louisia, S.; Yu, S.; Jin, J.; Roh, I.; Chen, C.; Pollock, C. J.; Huang, X.; Shao, Y.; Wang, C.; Muller, D. A. Operando Studies Reveal Active Cu Nanograins for CO_2 Electroreduction. **2023**, *614* (March 2022). https://doi.org/10.1038/s41586-022-05540-0.

(45) Yae, S.; Sakabe, K.; Fukumuro, N.; Matsuda, H. New Surface-Activation-Process for Electroless Deposition of Adhesive Metal (Ni, Cu) Films on Si Substrates. *ECS Meeting Abstracts* **2010**, *MA2010-02* (31), 1966–1966. https://doi.org/10.1149/ma2010-02/31/1966.